The International Journal of Advanced Manufacturing Technology (2022) 118:3361–3373
https://doi.org/10.1007/s00170-021-08176-y

ORIGINAL ARTICLE

Optimising part quality in the flexible roll forming of an automotive component

Buddhika Abeyrathna[1] · Sadegh Ghanei[1] · Bernard Rolfe[2] · Richard Taube[3] · Matthias Weiss[1]

Received: 10 May 2021 / Accepted: 3 October 2021 / Published online: 14 October 2021

Abstract
Roll forming is increasingly used in the automotive industry for the manufacture of structural and crash components from ultra-high-strength steel (UHSS). Springback and end flare are common shape defects in roll forming and increase with material strength. The conventional roll forming process is limited to the manufacture of components with a uniform cross section while flexible roll forming can produce parts with variation in width and depth. In this paper, the flexible roll forming of an automotive component from three different high-strength sheets of steel is investigated. The experiments are carried out with a flexible roll forming prototyping facility and combined with finite element analysis. The study shows that the flexible roll forming of high-strength automotive components is possible. Springback and end flare depend on the material strength and the forming sequence and can be reduced with a flexible forming approach where the material is first overbent followed by bending back. Wrinkling of the flange was observed but the severity of wrinkling reduced with an increasing number of forming passes.

Keywords Roll forming · Flexible roll forming · Springback · End flare · Finite element analysis · High-strength steel

1 Introduction

More than 20% of the greenhouse gas emissions are due to road transportation [1], and the automotive industry has been under increasing pressure to reduce the weight of the body in white. This has led to the increased use of advanced high- and ultra-high-strength steels (AHSS and UHSS).

The forming of higher strength steels with conventional cold stamping is difficult while hot stamping is costly and requires complex process design [2]. Roll forming is a low-cost process and has been increasingly used in the automotive industry for the manufacture of structural parts. In roll forming, a profile is incrementally formed by passing a flat sheet through a consecutive set of rolls. The dominant deformation mode in roll forming is bending, and this allows the forming of materials with limited ductility [3]. Shape defects and springback can be compensated with flexible approaches and this suits the forming of higher strength steels [4, 5]. However, roll forming is limited to the forming of long components with a constant cross section while, in the automotive industry, parts need to be structurally optimised and require a variation of the cross section over the length.

In flexible roll forming (FRF), the forming rolls are no longer fixed in space but can translate and rotate to form components that vary in width and depth over the length of the component [6]. Full part families can be formed with limited tool change required; this reduces costs. Abee et al. [7] have investigated the FRF of profiles with variable cross sections in width while in [8] automotive components such as crash barriers, frame members and bumpers were proposed as potential technology candidates. A bus frame component was successfully manufactured by flexible roll forming in Kim et al. [9].

The major shape defects in FRF are web warping, which is the height deviation of the web as well as wrinkling in the flange [10]. Web warping has been extensively investigated in the literature and increases with material strength [11] and part complexity [12]. Some techniques were introduced to reduce web warping. These include the heating of the critical flange regions [13], a blank holder [7, 14] to support the

✉ Buddhika Abeyrathna
buddhika.a@research.deakin.edu.au

1 Institute for Frontier Materials, Deakin University, Waurn Ponds, Pigdons Rd., Geelong, VIC 3216, Australia

2 School of Engineering, Deakin University, Waurn Ponds, Pigdons Rd., Geelong, VIC 3216, Australia

3 Ford Motor Company of Australia Ltd, 1735 Sydney Rd., Campbellfield, VIC 3061, Australia

web, overbending of the flange [15] and the optimisation of the bend curve [6]. Only a few studies have aimed at reducing flange wrinkling. These investigations proposed special roll tooling [10, 16] and a blank holder solution [17] but wrinkling remains a major issue in the FRF process.

End flare is a common shape defect in roll forming and generally occurs due to residual stresses that are released during material cutoff. It can also appear in the roll forming of a pre-cut strip and generally reveals itself by a distortion of the cross section at the component ends [18]. A previous study focussed on controlling end flare in flexible roll forming by overbending with a variable tool path. This approach allowed to apply a higher overbending angle at the component ends and successfully compensated for end flare [19].

A prototyping FRF facility has been recently established [20] that enables the forming of components of variable depth and width from AHSS and UHSS. The facility simulates the forming conditions present in FRF and can be used to develop solutions for shape control [17]. In this study, the facility is used in combination with numerical analysis to further understand wrinkling, end flare and springback in the flexible roll forming of an automotive component. Based on the results, solutions for shape control are developed and experimentally validated.

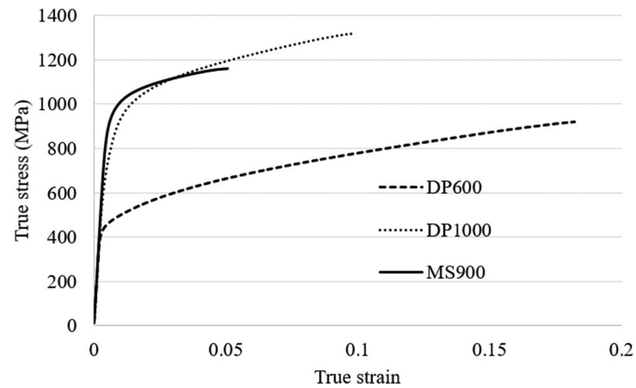

Fig. 1 Averaged true stress–strain curves determined along the rolling direction for the three sheets of steel

2 Materials and component shape

Two dual-phase and one martensitic steel, designated DP600, DP1000 and MS900 respectively, were investigated. All steels had a material thickness of 2 mm. Tensile tests were performed with a 30-kN Instron 5967 tensile tester, according to ASTM E8/E8M [21] on samples oriented in the rolling direction. A test speed of 0.025 mm s^{-1} was used giving a strain rate of 0.001 s^{-1}. Three samples from each material were used and the averaged true stress–strain curve for all materials is shown in Fig. 1. The strength coefficient (K) and the strain hardening exponent (n) were obtained by fitting Hollomon's power law equation to the true stress-effective plastic strain curves and the corresponding values are given in Table 1.

The symmetric half of the component selected for this study is shown in Fig. 2a; this is a modified version of an automotive component. The profile thickness is 2 mm. The cross section of the component varies in width along the length. The front cross section of the part is shown in Fig. 2b. The critical radii of the pre-cut blank that result in the highest longitudinal tension and compression in the flange are 243.3 mm and 318.9 mm respectively and are shown in Fig. 2c. To calculate the theoretical strain, Eq. (1) was used with the corresponding parameters shown in Fig. 2d.

$$\varepsilon_{th} = \ln\frac{R_0 \pm F(1 - cos\varphi)}{R_0} \quad (1)$$

where R_0, F and φ are the curve radius of the pre-cut, the effective flange length and the forming angle.

Figure 2 a shows the critical regions in the left and the right flange with the corresponding maximum theoretical strains indicated before and after the top hat in the left flange is formed. It can be seen that the left and the right flanges undergo tension and compression deformation, respectively.

3 Experimental flexible roll forming trials

The important parts of the facility used for the flexible roll forming trials of this study are shown in Fig. 3. First, the pre-cut blank is positioned and clamped between the top and bottom die. The top die includes the inner features of the part to be formed. A clamping force is applied by eight hydraulic cylinders on the top die; then, the carriage which holds the two dies is driven back and forth by a servo motor attached to a lead screw. At the same time, the forming tools mounted on either side of the clamps are changing their position and rotate to follow the part contour and to form the flanges to the required angle. The whole part is formed in multiple passes and with several forming tools. The control programme uses the part contour to define the tool orientation and movement during each forming step. The tool path is established with the features of the forming die as explained in Abeyrathna

Table 1 Material properties determined with the fitted Hollomon's law for DP600, DP1000 and MS900

Material	Yield strength (MPa)	Ultimate tensile strength (MPa)	Elastic limit	n	K (MPa)
DP600	446.5	767.7	0.0022	0.117	926.3
DP1000	764.1	1194.3	0.0038	0.122	1632.8
MS900	931.9	1102.7	0.0047	0.058	1337.8

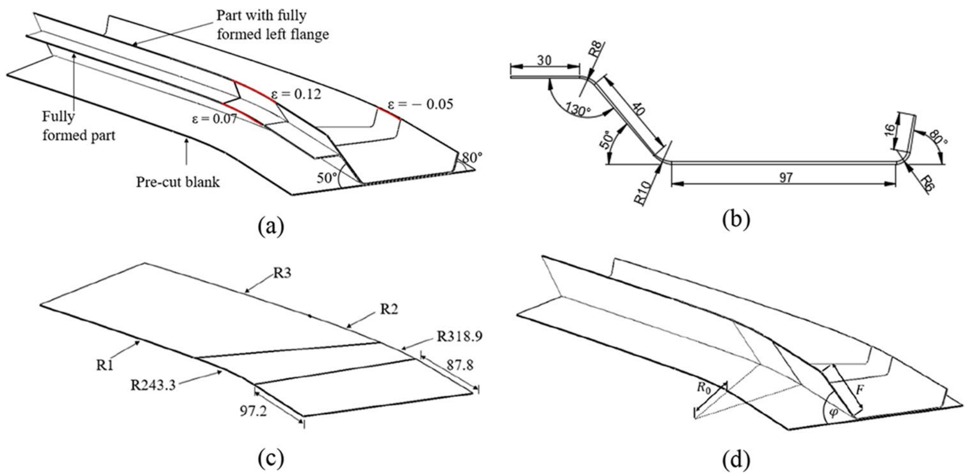

Fig. 2 **a** Schematic of the symmetric half of the component and with the theoretical strains in the critical forming regions, **b** cross-sectional view, **c** critical radii of the pre-cut blank, **d** part shape parameters considered for the analytical calculation of theoretical longitudinal strain

et al. [22] and used to form the flange as it is shown in Fig. 3. The forming procedure is different to conventional FRF where multiple roll stands are equipped with top and bottom forming rolls that can translate and rotate to follow a flexible part contour. Here a pre-cut sheet is pulled through the roll former by the rotation action of the forming rolls and friction. This can lead to a mismatch in roll rotation speed and sheet movement, especially in the part contour transition zones and can lead to surface quality issues. In the new process, a clamped sheet is moved through one set of forming rolls that are free to rotate. This reduces surface damage.

Two different forming sequences were used to form the left and the right flanges. The constant radius forming approach is employed in which the segments of the arc element are bent into the final radius in each forming step while keeping the bending radius the same [18]. In forming sequence 1 (FS1), the left flange is formed in 3 passes with 20°, 20° and 10° angle increments while, for the right flange, 4 passes with 20° equal angle increments (see Fig. 4a) are used. Forming sequence 2 (FS2) used two passes of 20° and 30° angle increment for the left flange and three angle increments of 20°, 30° and 30° for the right flange (see Fig. 4c). The top hat on the left flange was formed in both forming cases in five passes using angle increments of 18°, 8°, 8°, 8° and 8° (see Fig. 4 b and d).

Two bottom rolls were used to form the left flange to 50° while one bottom roll was used to form the right flange to 80° as shown in Fig. 5a. This was followed by a tool change and the forming of the top hat with profiled top and bottom rolls (see Fig. 5b).

One objective of this study is to understand the effect of material properties and the forming sequence on wrinkling severity. The part shape and wrinkling were evaluated on the right flange as it undergoes compressive deformation, which led to edge wrinkles. For that, the outer surface of the formed part was scanned with a HandyScan 3D [23] and the deformation of the flange was evaluated by performing a section cut through the flange edge with Geomagic Qualify [24] (see Fig. 6). For that, a section cut perpendicular to the formed flange and located 2 mm from the edge was considered as shown in Fig. 6a. To have a quantitative measure of the flange edge wrinkles, the mean absolute error (MAE) of the flange edge was evaluated using Eq. (2). For that, the deformed flange edge was compared with the ideal shape of the flange edge in the critical region (at a *Z*-coordinate of 70 to 320 mm from the front edge of the component) where most of the wrinkles were observed (see Fig. 7). For that, the scanned surface was manually aligned with the ideal part to minimise the error due to springback.

$$\mathrm{MAE} = \frac{1}{n}\sum_{i=1}^{n}\left|x_i - \hat{x}_i\right| \tag{2}$$

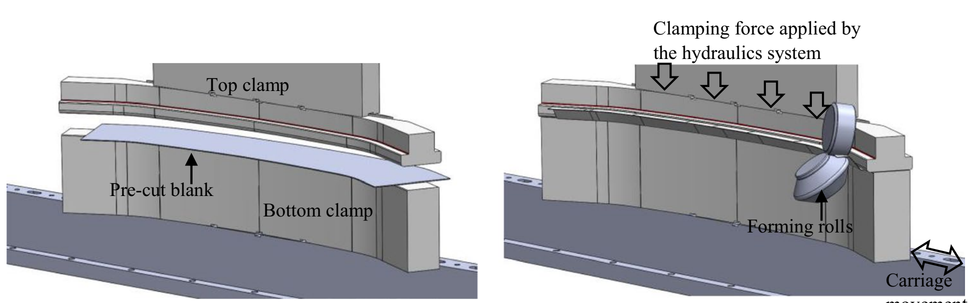

Fig. 3 Schematic indicating the forming approach of the prototype flexible roll forming facility

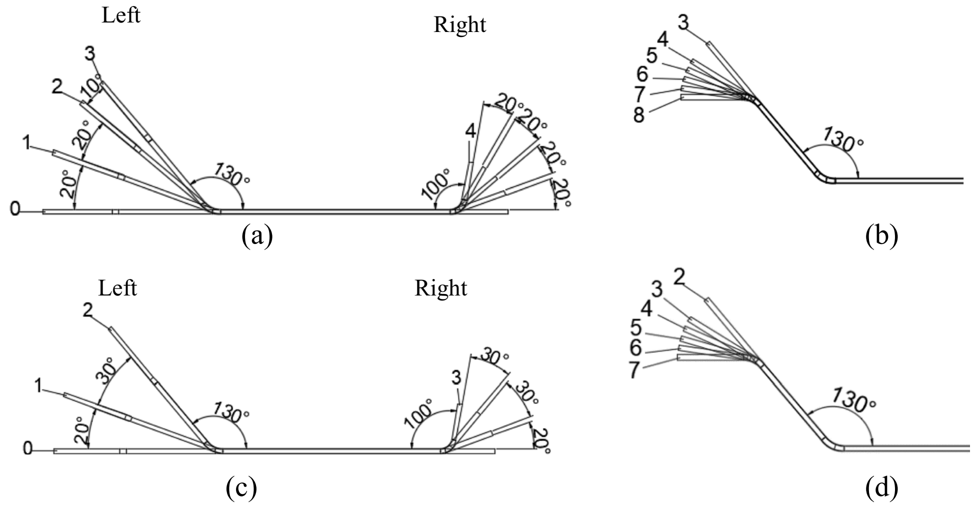

Fig. 4 Bend progression in **a** flange forming with FS1, **b** hat forming with FS1, **c** flange forming with FS2, **d** hat forming with FS2

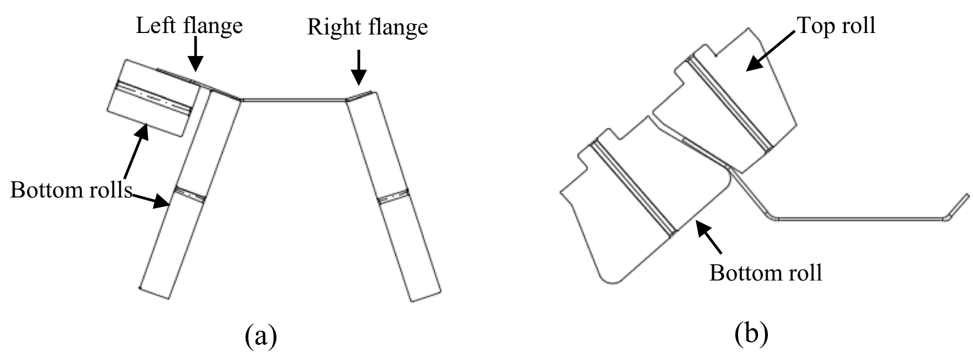

Fig. 5 The roll tooling that was used to form **a** the left and right flanges, **b** the top hat on the left flange

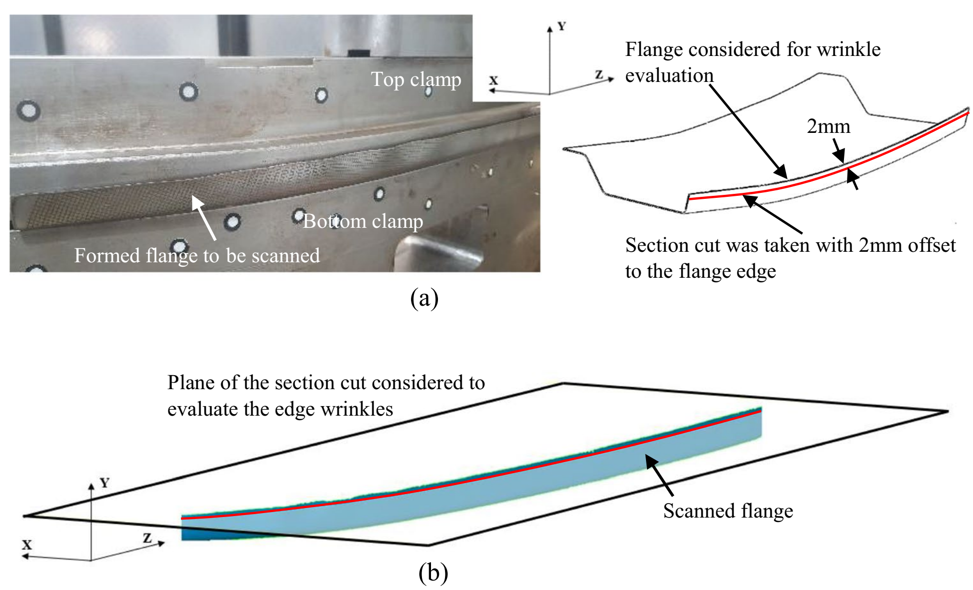

Fig. 6 **a** Formed right flange, **b** wrinkling evaluation over the selected (red) cross-section length

where x_i is the X coordinate of the deformed flange edge, $\hat{x}_i$ is the corresponding X coordinate of the ideal flange edge and n is the number of measuring points.

The longitudinal edge strain was evaluated on the left flange at a forming angle of 50° and before the hat was formed, as the flange undergoes the maximum longitudinal

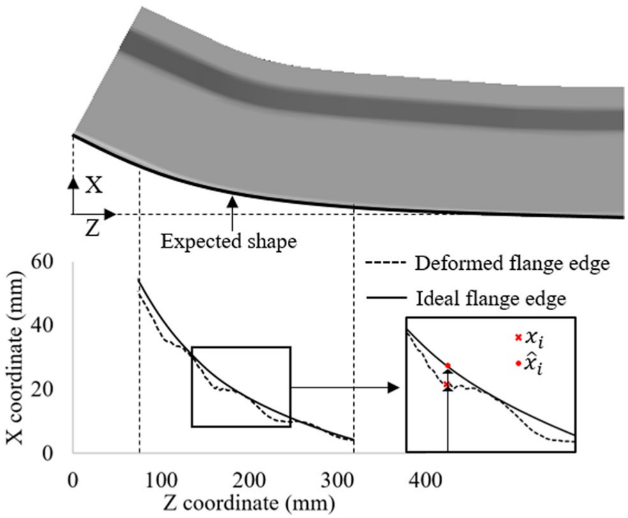

Fig. 7 Flange edge considered for wrinkling analysis

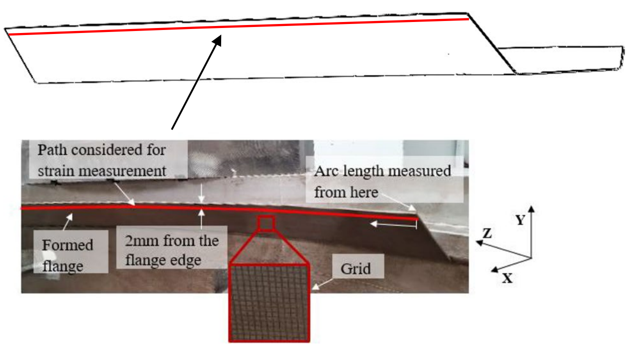

Fig. 8 Formed left flange where the longitudinal strain was measured with the AutoGrid Compact DIC system

tension at this stage (see Fig. 2a). The strain measurements were carried out with an AutoGrid Compact strain measuring system [25]. For this, the pre-cut blank was etched with a 2 mm × 2 mm grid and pictures taken on the flange after forming with the part being still fixed between the top and the bottom die. The true major strain was evaluated along a path located with a 2-mm offset to the flange edge of the front half, as shown in Fig. 8 and two samples were tested for each material type.

Another objective of this study is to identify the effect of material properties on springback and to introduce a solution for springback compensation. For this, springback in the three formed angles (α, β, θ in Fig. 9) was experimentally evaluated. This was done for condition FS1 only as there was severe wrinkling in the right flange for FS2. For the springback measurement, 2 cross sections were considered at the front (S1) and centre length (S2) of the sample. First, the left and the right flanges were formed up to 50° and 80° respectively, as it is shown in Fig. 9 a. Then, the angle of the flanges was measured while the formed part was held between the clamps. For that, the scanned surface with the 3D scanner and transverse section cuts in the Geomagic software were considered as explained above. After this, the top hat was formed to 50° on the left flange (see Fig. 9 b) and the angle after springback was measured. A schematic of the springback at the bend corresponding to angle, α, is shown in Fig. 10. The springback is the difference between the ideal angle and the angle after forming as given by Eq. (3). Based on the determined springback angles, an additional forming pass was introduced to overbend the flanges. The tool orientation for the overbending of the different angles is shown in Fig. 11 and the overbending angle at angles α, β and θ was considered as $\hat{\alpha}$, $\hat{\beta}$ and $\hat{\theta}$ respectively. For the overbending, a trial and error approach was used. The measured springback angle was used as the baseline and the overbending angle gradually increased until the ideal angle was achieved. In addition, a bending back (BB) forming step was introduced for the forming of the hat bending angle θ. For that, the last hat forming pass was repeated after the overbending pass. All springback measurements occurred while the part was held between the two clamps. The measured springback angles at S1 and S2 were used to determine the end flare angle. The end flare angle was defined as the difference between the measured angle between S1 and S2 as given by Eq. (4).

$$\Delta\alpha = \alpha - \acute{\alpha} \tag{3}$$

where $\Delta\alpha$ is the springback angle, α is the ideal flange angle and α is the measured flange angle after forming

$$\alpha_{EF} = \Delta\alpha_{S1} - \Delta\alpha_{S2} \tag{4}$$

where α_{EF} is the end flare corresponding to forming angle α and $\Delta\alpha_{S1}$ and $\Delta\alpha_{S2}$ are the springback angles corresponding to S1 and S2 respectively.

Fig. 9 Measured angles after **a** flange forming, **b** hat forming

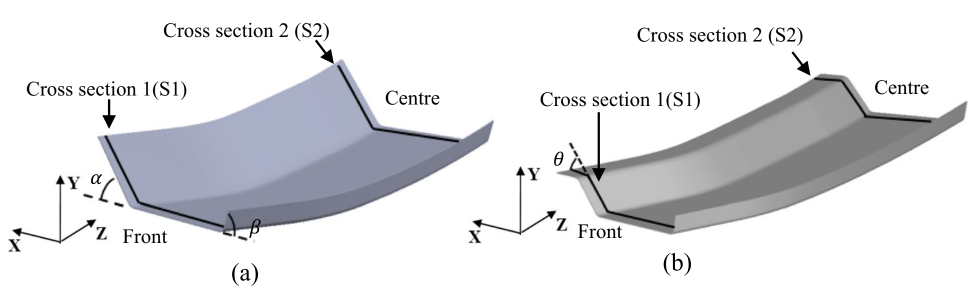

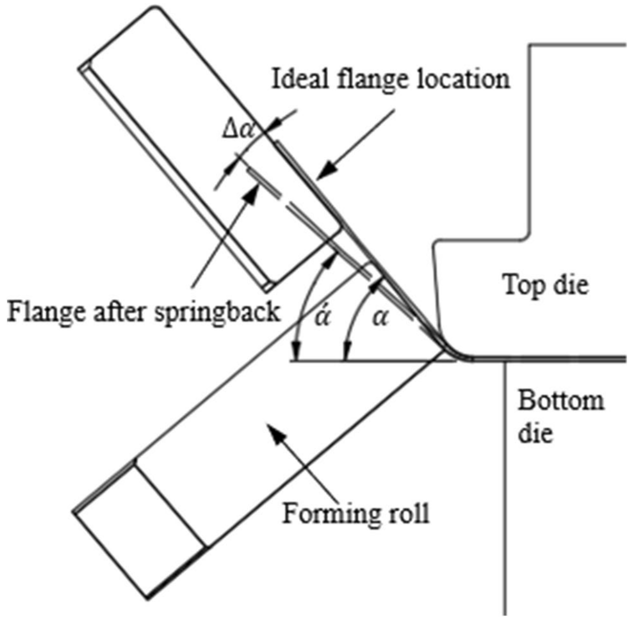

Fig. 10 Definition of springback for angle α

4 Finite element analysis

The flexible roll forming process was simulated with the commercial software package Copra FEA RF [26], which uses an implicit solver. While in the real process, the carriage with the top and bottom clamps and the pre-cut blank move back and forth through one single forming station, in the finite element model, the pre-cut blank and the clamps are fixed while the forming rolls move over the sheet to form it into shape (see Fig. 12 a). The two clamps and the forming rolls were modelled as rigid bodies and the pre-cut blank discretised with full integration, hexahedral, type 7, arbitrarily distorted brick elements [27]. A frictionless contact was assumed between the rolls and the blank [22]. The mesh was refined in the bending regions and two layers of elements were used through the material thickness. Only one longitudinal half of the pre-cut blank was modelled due to symmetry (see Fig. 12 b). Elastic material behaviour was defined assuming an E-Modulus of 200 GPa and Poisson's ratio of 0.3 [22]. The plastic components of the true stress-true strain curves shown in Fig. 1 were used together with isotropic hardening and the von Mises yield criterion to define plastic material behaviour.

Three boundary conditions were applied to the blank and are shown in Fig. 12 b. An X lock was applied to all nodes along the centre line to restrict material movement in the *X* direction during forming. A Y lock was applied on three nodes at the bottom end of the sheet during clamping to hold the sheet until the clamps come together and secure it. All measurements were taken with the sheet being clamped as in the experiments. A Z lock was applied on all nodes at the symmetric centre and on three nodes at the front to prevent any material movement in the *Z* direction during forming. Two nodes were assigned to each forming roll and used to define their tool paths and angles.

The shape of the formed part in the FEA was evaluated with Geomagic Qualify [24] using the same procedure as explained in Sect. 3. To evaluate the strain, a node path at the left flange edge, on the bottom surface of the formed flange, was considered as it is shown in Fig. 13a. The plastic component of longitudinal strain was compared with the experimental results for the front half at 50° of flange bending. To understand the evolution of longitudinal stress, a node in

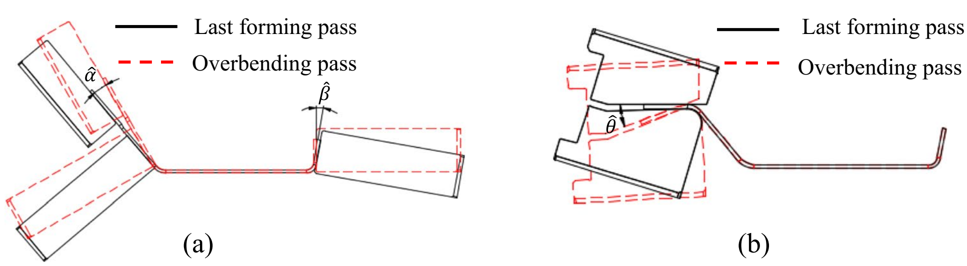

Fig. 11 Tool orientation in the last forming pass and overbending for angles **a** α and β, **b** θ

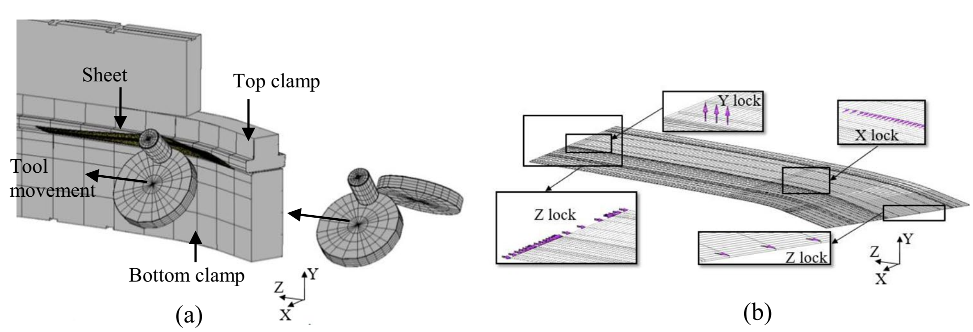

Fig. 12 **a** Finite element model assembly, **b** boundary conditions on the pre-cut

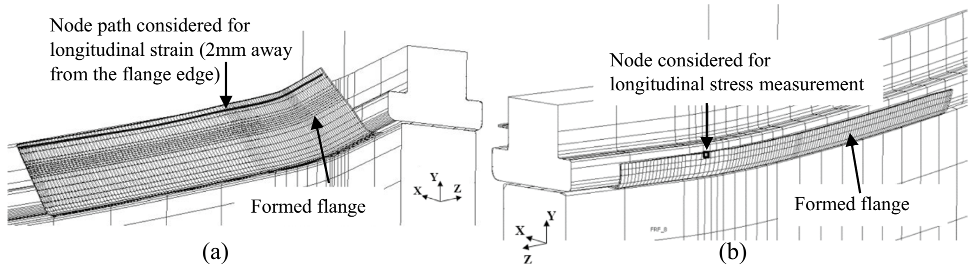

Fig. 13 **a** The node path considered for the analysis of longitudinal strain, **b** the node considered for the analysis of longitudinal stress

the critical region of the right flange edge was considered as shown in Fig. 13b.

5 Results

5.1 Wrinkling

The EXP and the FEA results for the shape of the right flange for FS1 and FS2 are shown for a final bending angle of 80° in Fig. 14a and b respectively (as explained in the procedure corresponding to Fig. 6 and Fig. 7). A 10-mm *X* coordinate offset is applied between the three materials for better illustration. The FEA gives a good representation of the level of edge wrinkling observed in the experiments for both forming sequences; there is only a slight difference in the wrinkling pattern. The evaluated mean absolute error (MAE) values for the experiments and the FEA are given in Fig. 14c. There is a good agreement between the FEA and the experiments regarding the magnitude of the wrinkles for FS2, while the FEA slightly underestimates wrinkling for FS1. The deviation between the FEA and the experimental result may be related to the gap between the forming roll and the top die being larger than the sheet thickness due to tool deflection which has not been considered in the FEA. This may explain the differences in wrinkling severity and wrinkling pattern observed between the EXP and the FEA for FS1 and FS2 respectively. The wrinkles appeared after the second forming pass at a forming angle of 40° and 50°for forming sequences FS1 and FS2 respectively irrespective of the material type. However, at the final forming angle of 80°, FS2 showed higher wrinkling severity than FS1 (Fig. 14a and b). In addition, the wrinkling severity clearly increased with material strength in FS2 while there is only a minor effect of material strength for FS1.

5.2 Material deformation in the flange

The distribution of longitudinal residual strain along the arc length of the critical region in the left flange at a forming angle of 50° (before the forming of the hat was started) is shown for FS1 and FS2 in Figs. 15 and 16 respectively. The strain

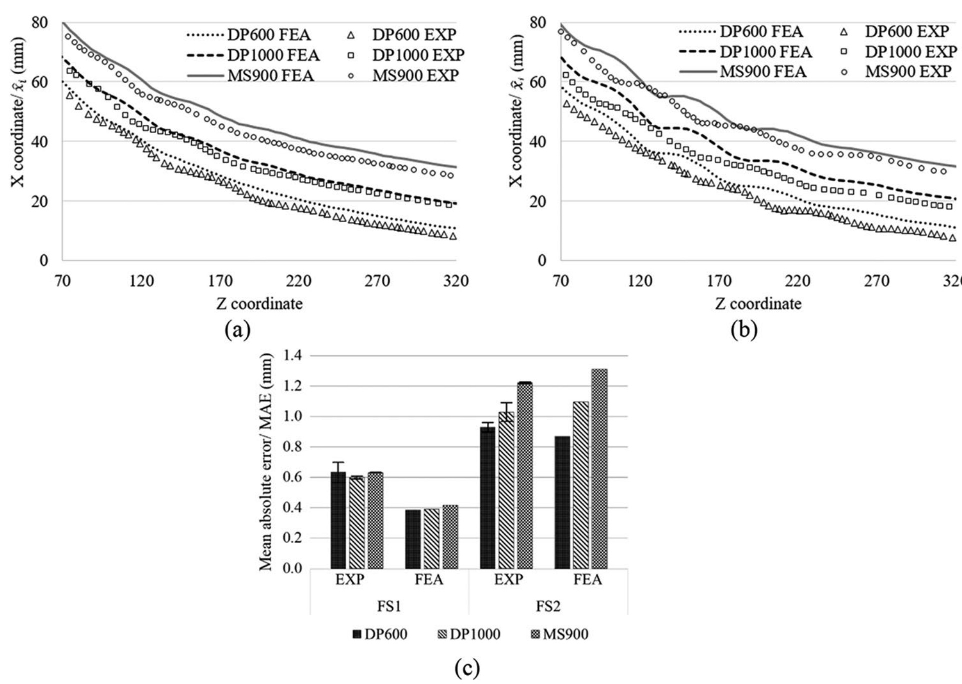

Fig. 14 **a** Comparison of the flange edge distortion for FS1, **b** comparison of the flange edge distortion for FS2, **c** MAE of the flange edge for FS1 and FS2

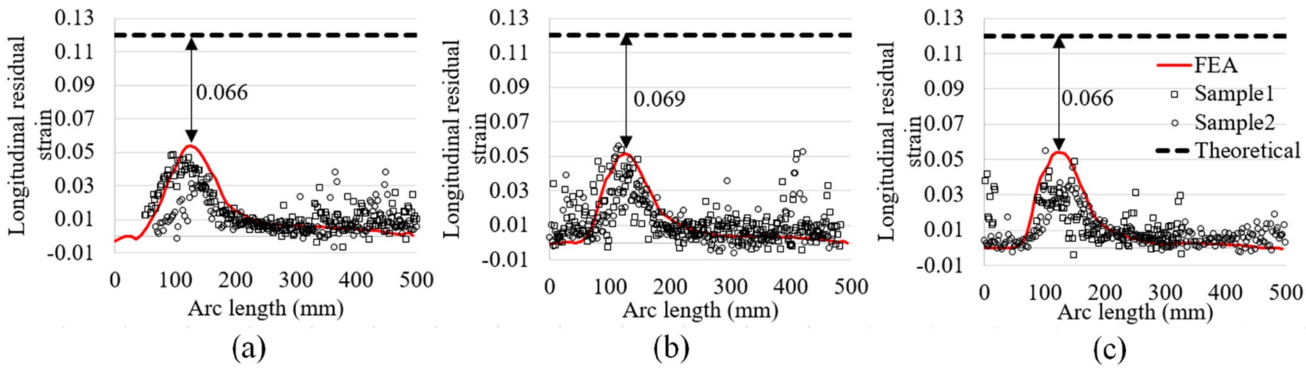

Fig. 15 Longitudinal residual strain along the left flange edge after a bending angle $\alpha = 50°$ for FS1 and **a** DP600, **b** DP1000, **c** MS900

measurements for two samples (sample 1 and sample 2) are compared with the FEA results for each material and forming case. The strain reaches a maximum of approximately 135-mm arc length. There is no significant difference in the peak strain between the three materials and the two forming sequences FS1 and FS2. The experimental results show some scatter especially at the regions with low strain. This is related to the limited accuracy of the AutoGrid system at low levels of strain. For most cases, the peak strain predicted by the FEA is slightly higher compared to that measured experimentally. Overall, the FEA and the EXP results suggest that neither the forming sequence nor the material properties have a significant influence on the level of permanent longitudinal strain. The left flange mainly undergoes tensile deformation in the longitudinal direction, and based on Eq. (1), the level of theoretical strain required to form the part shape is $\varepsilon_{th} = 0.12$ (see Fig. 2a). The results in Fig. 15 suggest that less than 50% of the required theoretical longitudinal tensile strain is permanently formed into the flange.

5.3 Springback and end flare

Figure 17 a shows the springback for forming sequence FS1 after bending the left flange ($\Delta\alpha$), the right flange ($\Delta\beta$) and the top hat ($\Delta\theta$). The DP1000 shows the highest springback while the lowest springback can be seen for DP600, which also has the lowest yield and flow stress. Springback after forming the top hat ($\Delta\theta$) is the highest given that the flange is unsupported during the forming process as it is shown in Fig. 5b. This lack of support likely results in, θ, not being fully formed and results in high springback.

The end flare determined with Eq. (4) is shown in Fig. 17b. The end flare was analysed on the right and left flanges before the top hat was formed. It can be seen that springback in the front section of the component, S1, is smaller than that in the middle section, S2, for the left flange (α) while the trend is opposite for the right flange (β). This indicates that material flares out at the left flange but flares in at the right flange.

5.4 Compensation

The overbending angles were determined based on the highest value for springback determined in sections S1 and S2 and are shown in Table 2. However, this is a trial and error approach where the overbending was performed until the required part geometry was achieved. Table 2 therefore

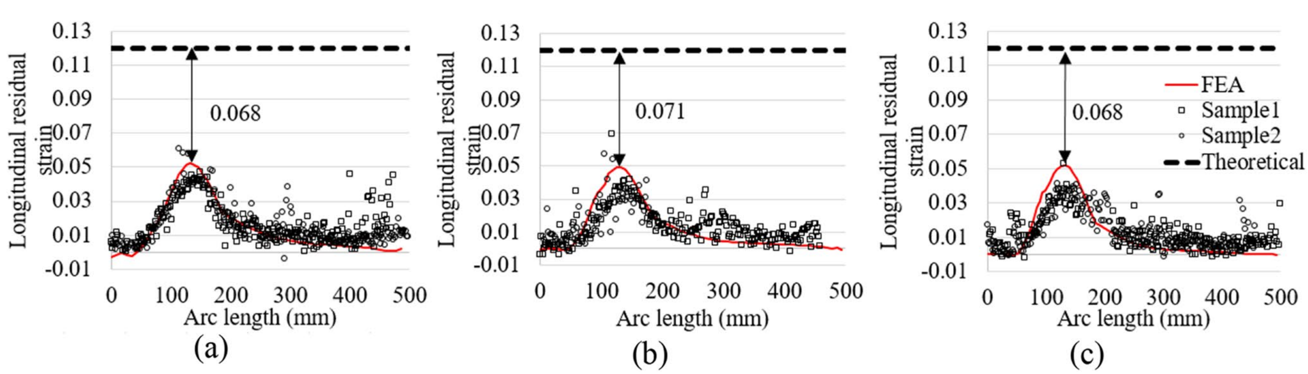

Fig. 16 Longitudinal residual strain along the left flange edge after a bending angle $\alpha = 50°$ for FS2 and **a** DP600, **b** DP1000, **c** MS900

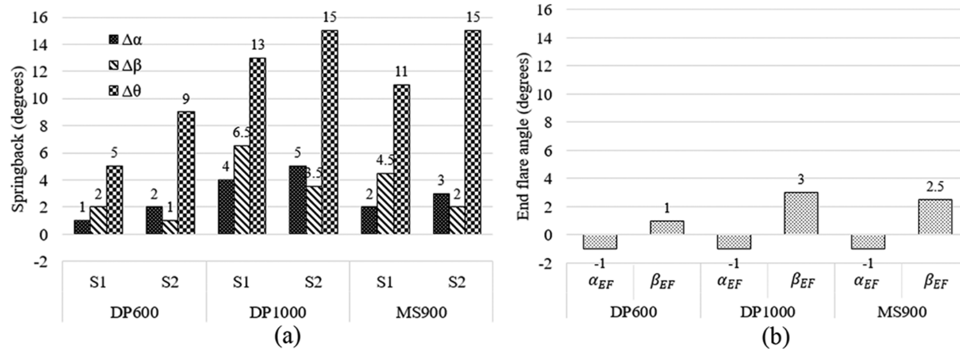

Fig. 17 **a** Springback in the left flange ($\Delta\alpha$) in cross sections S1 and S2 at 50°, right flange ($\Delta\beta$) at 80° and left flange ($\Delta\theta$) at 50° after the forming of the top hat **b** end flare measured using Eq. (4) in the left and the right flanges before the top hat is formed

shows the final overbending angle that resulted in the best possible part quality for the different materials. To overcome the issue of the lack of tool support when overbending the top hat (angle θ), an additional bending back forming step was applied as previously described.

The springback angle after overbending is shown in Fig. 18a and suggests that the overbending approach significantly improved the part quality in the flange and the top hat giving springback angles of ± 1°. A significant improvement in the top hat shape (angle θ) can also be observed. This suggests that springback in unsupported bends in FRF can be improved by an approach of overbending followed by bending back. The end flare distribution of the left and right flanges after overbending is shown in Fig. 18b. It can be seen that the end flare is also significantly reduced by the introduced overbending approach.

6 Discussion

6.1 The effect of material strength and forming sequence on the wrinkling tendency

The evolution of the longitudinal stress of a node in the critical region of the right flange (see Fig. 13b) is compared for all forming passes and for both forming sequences (FS1 and FS2) and the three different materials in Fig. 19a, b and c. The hypothesis is that wrinkling initiates when the compressive longitudinal stress in the flange edge reaches a critical value. Figure 19 d indicates the flange edge deformation when the forming roll is in contact with the sheet during the forming process. It can be seen in Fig. 19d that the flange edge follows a concave upward path followed by convex downward and reverse convex when the roll passes the flange similar to the flange edge movement in conventional roll forming as reported previously in Abeyrathna et al. [28]. This gives an initial compressive longitudinal deformation which is followed by tensile deformation and then compression as it is indicated by the FEA predictions for longitudinal stress for DP600, the DP1000 and the MS900 in Fig. 19a, b and c respectively.

According to Fig. 14c, the DP600 and the MS900 show the lowest and the highest edge wrinkling in the right flange respectively for both the FS1 and the FS2 forming conditions. This suggests that the wrinkling tendency increases with material strength. This may be related to the different levels of compressive stress that are developed in the flange when the materials are deformed. According to Groche et al. [29], the critical wrinkling initiation stress (σ_{crit}) in a variable width component can be estimated with:

$$\sigma_{crit} = \frac{\mathrm{k} \times \pi^2 \times E \times t^2}{12 \times \left(1 - \vartheta^2\right) \times F^2} \quad (5)$$

where, k, E, t, F and ϑ are the buckling factor, Young's modulus, the thickness, the flange length and Poisson's ratio respectively.

According to Eq. (5), the critical wrinkling stress is influenced by the geometry and the material properties. In Groche et al. [29], the buckling factor is considered to be 0.42 for a component with a similar transition radius and flange height as analysed here. Assuming Young's modulus of $E = 200$ GPa, this gives critical wrinkling stress of − 1186 MPa in the right flange which is indicated in Fig. 19a, b and c by the dotted line.

To investigate the wrinkling tendency, the level of the developed compressive stress, σ_{com}, in the right flange and the ratio of the compressive stress and the critical wrinkling stress were determined. In the first forming pass of FS1 and FS2 (at 20°), the flange edge undergoes compressive stress of $\sigma_{com} = 595$ MPa, 1009 MPa and 1078 MPa for the DP600, the DP1000 and the MS900 respectively. This gives ratios of compressive to critical wrinkling stress of $\frac{\sigma_{com}}{\sigma_{crit}} = 0.50$, 0.85 and 0.91 for the DP600, the DP1000 and the MS900, respectively. Based on the theory, wrinkling initiates when

Table 2 Final overbending angles that were used for springback compensation

	$\hat{\alpha}(°)$	$\hat{\beta}(°)$	$\hat{\theta}(°)$
DP600	3	3	9
DP1000	7	7	16
MS900	5	5	15

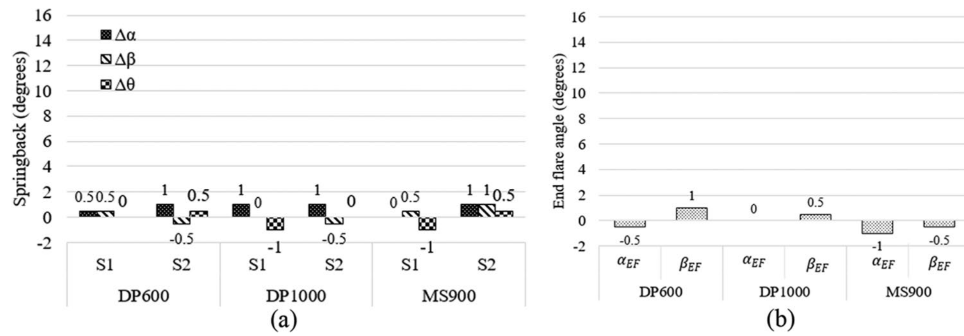

Fig. 18 **a** Final springback after overbending in the left flange ($\Delta\alpha$) in cross sections S1 and S2 at 50°, right flange ($\Delta\beta$) at 80° and left flange ($\Delta\theta$) at 50° after forming of the top hat **b** end flare after overbending in the left and the right flanges before forming the top hat

$\frac{\sigma_{com}}{\sigma_{crit}} > 1$ This suggests that the MS900 will reach the critical wrinkling stress first, followed by the DP1000, and then, the DP600 material, i.e., wrinkling severity, should increase with increasing material strength as it has been observed in Fig. 14a and b. However, the above analysis assumes a constant buckling factor, k, that is independent of the material properties [29]. As mentioned earlier, all materials showed buckling in the second forming station for both forming sequences FS1 (at 40°) and FS2 (at 50°). Figure 19 a, b and c present the longitudinal stress distribution during the process for the selected node in the critical region of the right flange for DP600, DP1000 and MS900 respectively. P1, P2, P3 and P4 indicate the time when the forming roll passes that particular node in the first, second, third and fourth forming pass. According to Fig. 19b and c, both the DP1000 and the MS900 exceed the critical stress level in the second station in FS2. For the MS900, the level of compressive stress that exceeds the critical stress level is higher compared to DP1000 and this may explain why the MS900 wrinkling is more severe.

However, as it can be seen in Fig. 19 a, the longitudinal compressive stress in the flange edge does not exceed the critical stress for the DP600 steel for both forming sequences even though experimentally and numerically wrinkling was observed. Also, for forming sequence FS1, both the DP1000 and the MS900 do not show compressive stress that exceeds the critical stress level even though both sheets of steel showed clear wrinkling initiation after forming pass 2 in both the FEA and the EXP. This may suggest that the real wrinkling limit stress is lower than the value calculated from Eq. (5). One potential reason for this could be the fact that the strip edge is not straight when it moves into the forming rolls but shows a pre-existing curvature that is governed by the variable-width contour that is formed. Such curvature would lead to a moment when a compressive stress is applied and would give a lower value for the critical wrinkling initiation stress (σ_{crit}) than calculated by Groche

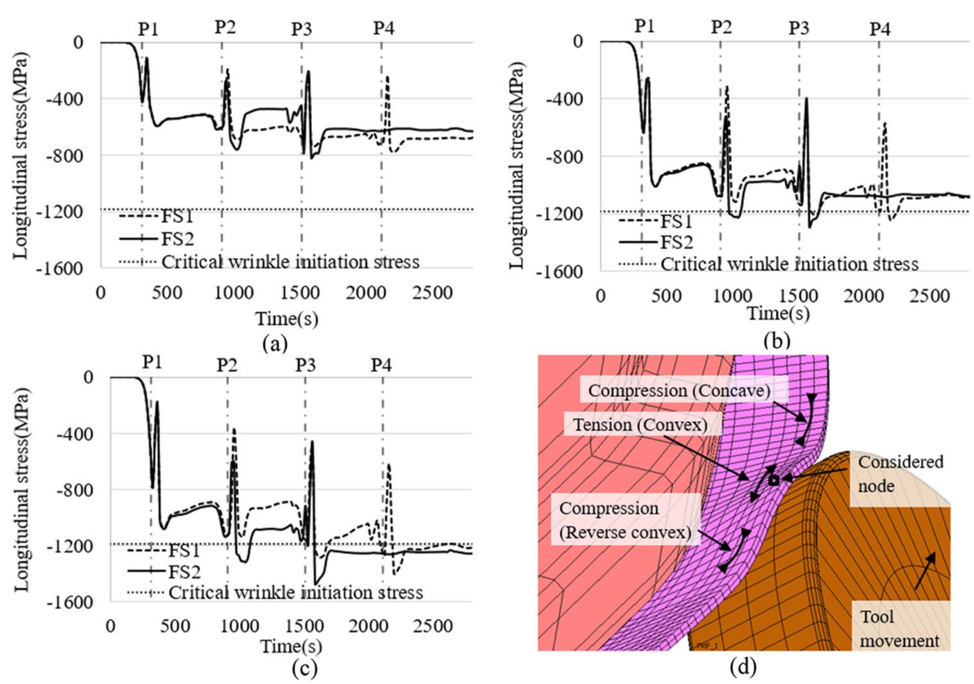

Fig. 19 **a** Evolution of longitudinal stress determined at a node in the critical wrinkling region of the right flange edge for DP600, **b** DP1000 and **c** MS900, **d** deformation of the sheet at the forming roll

et al. [29] which assumes a straight plate under compressive loading excluding any moment effects.

If a straight flange undergoes longitudinal compression as shown in Fig. 20a, the corresponding buckling limit can be estimated with Eq. (5). However, due to the part contour that is formed, there is a pre-existing curvature in the flange. If the flange undergoes longitudinal compression, then the resulting stresses lead to a bending moment that acts on the flange as shown in Fig. 20b. This reduces the critical longitudinal compressive stress that is required to initiate a winkle in the flange and potentially gives critical buckling stress that is lower than indicated by Eq. (5).

In addition to above, in the conventional roll forming process, there are 3 distinct deformation regions [28, 30] where the sheet first takes a concave, followed by a convex and then a reverse convex shape when it moves over the forming roll (Fig. 19d), i.e., the flange edge is not straight when it is formed over the roll. This could also explain why the longitudinal compressive stress that leads to winkling initiation in the flange, in the flexible roll forming process, is lower than that estimated with Eq. (5).

6.2 Causes of end flare in the left and the right flange

The results for longitudinal edge strain in Fig. 15 show that the tensile elongation of the left flange is only 50% of the theoretically required level. The left flange edge is therefore shorter than required and this results in the straight part of the left flange being pulled back by the adjacent arc material as schematically shown in Fig. 21a. According to Fig. 15a, all 3 materials show a similar mismatch between the theoretically required and the permanently formed longitudinal tensile

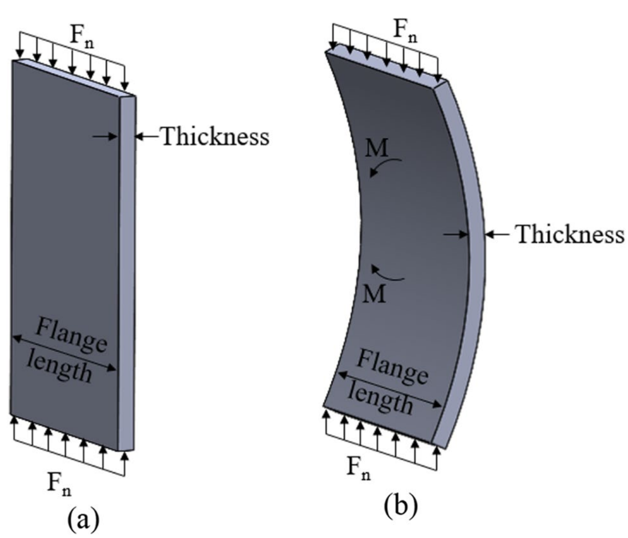

Fig. 20 Schematic of a **a** straight plate, **b** plate with pre-existing curvature undergoes longitudinal load

strain in the critical arc region, $\Delta\varepsilon = 0.066$. The corresponding missing arc length, Δl, can be calculated with Eq. (6) below. The arc length, l, of the critical region is 93.2 mm (from the pre-cut in Fig. 2c) which results in an undeformed length, Δl, of 6.2 mm (see Fig. 21a). If the last straight region is pulled back by 6.2 mm, the flange moves outward from the ideal position which leads to the flaring out effect.

The difference between the theoretical and the experimental longitudinal tensile strain that is formed in the left flange is the same for all 3 materials (Fig. 15) and this explains why all materials show the same level of end flare in the left flange (see Fig. 17b).

In the right flange, wrinkling was observed in the critical forming and wrinkling severity increased with material strength (see Fig. 14a and c). The compressive stresses in the critical forming region of the left flange lead to the straight entity being pulled back by the advanced critical forming region, this time moving inward from the ideal position (see Fig. 21b). The degree of inwards flare in the right flange increases with material strength as shown in Fig. 17b where the end flare is higher for the DP 1000 and the MS 900 compared to the lower strength DP600. This is due to the lower wrinkling severity observed in the DP 600 compared to the two higher strength sheets of steel which leads to less shortening of the critical area (Fig. 14a and c).

$$\Delta l = \Delta\varepsilon \times l \quad (6)$$

7 Conclusions

In this study, the flexible roll forming of an automotive component with variable width was analysed using a new flexible roll forming prototype facility. Three types of advance high-strength steel (AHSS) were investigated in combination with two different sequences of bending, one for severe forming and the other representing a smoother forming approach with a larger number of forming steps and smaller bending increments. The effect of material strength and forming sequence on the wrinkling tendency, springback and end flare was investigated and an approach for springback and end flare compensation was developed and experimentally validated.

The following conclusions can be made:

- Flexible roll forming enables the manufacture of longitudinal components from high- and ultra-high-strength steels. In this study, for the first time, the flexible roll forming of an automotive component from DP1000 and MS900 steel was experimentally validated.
- One major process limitation when flexible roll forming higher strength steel is excessive wrinkling in the flange. This study suggests that wrinkling severity increases with

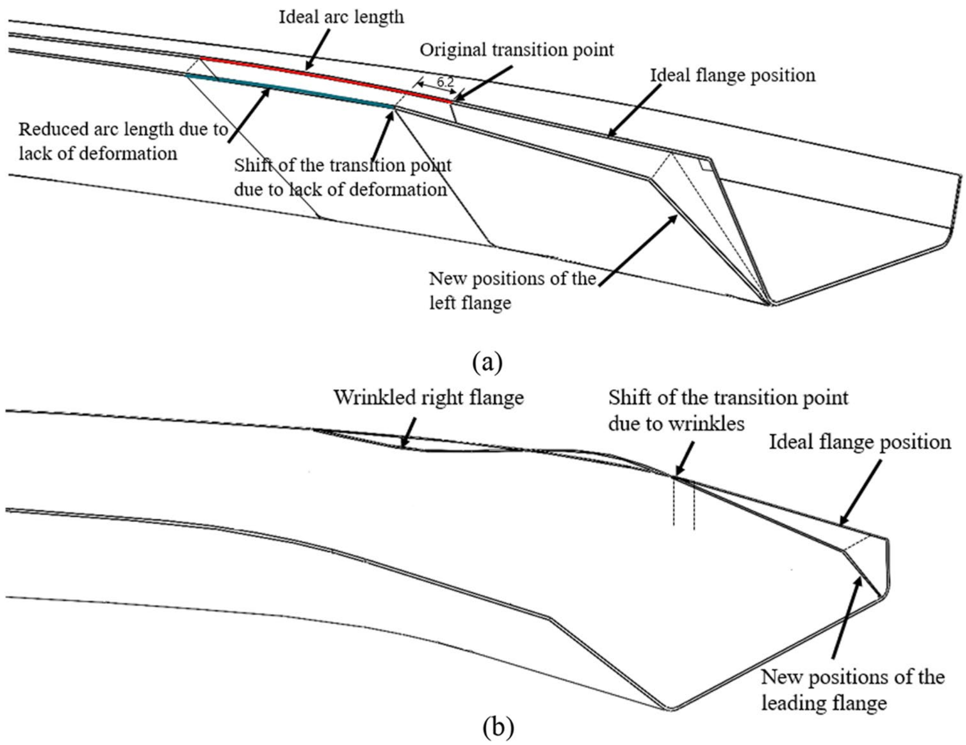

Fig. 21 Schematic of the deformation of the **a** left flange, **b** right flange

material strength but reduces with an increasing number of forming passes, i.e., a lower bending angle increment that is formed. Increasing the number of forming passes in flexible roll forming therefore represents a promising solution to achieve a wrinkle-free component. Future investigation is required to fully understand the potential of this method to eliminate wrinkling initiation.

- A higher material strength increases the compressive stress in the flange reaching the critical wrinkling initiation stress earlier, giving higher wrinkling severity. When the number of forming passes is increased, the compressive stress in each individual forming pass is reduced and wrinkling initiation delayed.
- All materials showed wrinkling initiation before the critical wrinkling stress was reached. The critical wrinkling stress is commonly calculated by the plate buckling theory which neglects the effect of a bending moment. This study showed that when the material enters the forming roll there is a pre-existing curvature which may result in bending moment effects and the reduction of the critical wrinkling stress.
- All materials showed significant end flare. The results of this study suggest that the end flare defect is the result of the shorting of the flange edge. On the left side, the shorting of the flange is due to an insufficient forming of material while in the right flange it results from flange wrinkling.
- A simple overbending and bending back approach is presented and it is experimentally shown that this approach almost compensates for end flare and springback defects. The presented flexible roll forming technology allows for the CNC controlled optimisation of the forming tool movement. A combination of in-line shape monitoring and flexible shape control may therefore be integrated in the future for quality management. In the current study, the flange was not supported when the top hat was formed (Fig. 5b). This led to the flange moving out of shape (angles β) when the top hat was formed. This defect can be reduced with a forming roll arrangement that provides full support of the flange during hat forming. Such a tool was not available in the current study.
- The class of materials that can be formed with the FRF process depends on the part geometry. If the flange edge only undergoes longitudinal tensile deformation, most AHSS and UHSS can be formed if the techniques for shape compensation presented in this study are applied. If there are flange regions that undergo compressive stress; then, the part quality reduces with increasing material strength. At a certain level of material strength, the part cannot be formed without wrinkles.

Acknowledgements The authors also acknowledge the technical and software support provided by data M Sheet Metal Solutions GmbH. The authors would further like to thank Emeritus Professor John Duncan for his assistance in writing this paper.

Funding The authors would like to thank ARC Training Centre in Lightweight Automotive Structure (project number IC160100032) and the Ford Motor Company (Australia and USA) for the financial support.

Availability of data and material Not applicable.

Code availability Not applicable.

Declarations

Competing interests The authors declare no competing interests.

References

1. Del Pero F, Delogu M, Pierini M (2017) The effect of lightweighting in automotive LCA perspective: estimation of mass-induced fuel consumption reduction for gasoline turbocharged vehicles. J Clean Prod 154:566–577
2. Hashmi S (2014) Comprehensive materials processing: Elsevier Science
3. Deole AD, Barnett MR, Weiss M (2018) The numerical prediction of ductile fracture of martensitic steel in roll forming. Int J Solids Struct 144–145:20–31
4. Abeyrathna B, Rolfe B, Hodgson P, Weiss M (2013) Sensitivity analysis of roll load, torque and material properties in the roll forming process. AIP Conf Proc 1567:900–903
5. Abeyrathna B, Rolfe B, Hodgson P, Weiss M (2016) A first step towards a simple in-line shape compensation routine for the roll forming of high strength steel. IntJ Mater Form 9:423–434
6. Rezaei R, Moslemi Naeini H, Tafti RA, Kasaei MM, Mohammadi M, Abbaszadeh B (2017) Effect of bend curve on web warping in flexible roll formed profiles. Int J Adv Manuf Technol 93:3625–3636
7. Abee A, Berner S, and Sedlmaier A (2008) Accuracy improvement of roll formed profiles with variable cross sections, presented at the ICTP 2008 (The 9th International Conference on Technology of Plasticity)
8. Wenting S, Qiang L, Bo Q (2011) Control strategy for the flexible roll forming machine with the structure of double rack and single gear, presented at the International Conference on Transportation, Mechanical, and Electrical Engineering (TMEE), Changchun, China
9. Kim D, Cha M, Kang YS (2017) Development of the bus frame by flexible roll forming. Procedia Eng 183:11–16
10. Abeyrathna B, Rolfe B, Pan L, Ge R, Weiss M (2016) Flexible roll forming of an automotive component with variable depth. Adv Mater Process Technol 2:527–538
11. Jiao J, Rolfe B, Weiss M (2013)The effect of tooling design parameters on web-warping in the flexible roll forming of UHSS, in AIP Conference Proceedings
12. Sun Y, Qian Z, Daniel WJT, Meehan PA, Shi L, Ding S (2017) Analytical and numerical analyses of the longitudinal plastic strain and web-warping in Chain-die-formed AHSS sections with variable widths. Int J Adv Manuf Technol 92:1147–1164
13. Larrañaga J, Berner S, Galdos L, Groche P (2011) Geometrical accuracy improvement in flexible roll forming lines. AIP Conf Proc 1315:557–562
14. Park JC, Yang DY, Cha MH, Kim DG, Nam JB (2014) Investigation of a new incremental counter forming in flexible roll forming to manufacture accurate profiles with variable cross-sections. Int J Mach Tools Manuf 86:68–80
15. Berner S, Storbeck M, Groche P (2011) A study on flexible roll formed products accuracy by means of FEA and experimental tests. AIP Conf Proc 1353:345–350
16. Abeyrathna B, Abvabi A, Rolfe B, Taube R, Weiss M (2016) Numerical analysis of the flexible roll forming of an automotive component from high strength steel. IOP Conf Ser Mater Sci Eng 159:012005
17. Ghanei S, Abeyrathna B, Rolf B, Weiss M (2019) Analysis of material behaviour and shape defect compensation in the flexible roll forming of advanced high strength steel. IOP Conf Ser Mater Sci Eng 651
18. Halmos GT (2006) Roll forming handbook. London Taylor & Francis
19. Abeyrathna B, Ghanei S, Rolfe B, Taube R, Weiss M (2020) Springback and end flare compensation in flexible roll forming. IOP Conf Ser Mater Sci Eng 012048
20. Sedlmaier A, Dietl T, Ferreira P (2017) Digitalization in roll forming manufacturing. J Phys Conf Ser
21. ASTM (2011) Standard test methods for tension testing of metallic materials, in https://www.astm.org, ed: ASTM International
22. Abeyrathna B, Rolfe B, Harrasser J, Sedlmaier A, Ge R, Pan L et al (2017)Prototyping of automotive components with variable width and depth. J Phys Conf Ser 012092
23. (2020, 13/01/2020). HandyScan3D. Available: https://www.creaform3d.com/en
24. (June 2014). Geomagic Qualify. Available: http://www.geomagic.com/en/
25. (2017, April 2017). ViALUX GmbH _ Autogrid. Available: https://www.vialux.de/en
26. Solutions dSM (2014) COPRA® RF - Software for Roll Forming, 2013 ed. Germany
27. (2020) Marc® User Manual, ed: MSC Software Corporation
28. Abeyrathna B, Rolfe B, Hodgson P, Weiss M (2016) Local deformation in roll forming. Int J Adv Manuf Technol 1–11
29. Groche P, Zettler A, Berner S, Schneider G (2011) Development and verification of a one-step-model for the design of flexible roll formed parts. IntJ Mater Form 4:371–377
30. Moneke M, Groche P (2021) Control of residual stresses in roll forming through targeted adaptation of the roll gap. J Mater Process Technol 294:117129